Electronic Research Archive

ERA, 34(12): 9267–9292.
DOI: 10.3934/era.2026390
Received: 21 June 2026
Revised: 17 September 2026
Accepted: 21 September 2026
Published: 29 October 2026

http://www.aimspress.com/journal/era

Research article

Design of Eyring-Powell fluid over a moving wedge using an artificial neural network: Statistical-based sensitivity with applications in aerodynamics

Muhammad Ramzan[1], Talal Taha[2], Ziwen Xu[1,*], Unai Fernandez-Gamiz[3], Yanhong Chen[1,*] and Abdulrahman A. Almehizia[4]

[1] Department of Astronautical Science and Mechanics, Harbin Institute of Technology, Harbin 150001, China
[2] Department of Mathematics and Statistics, Faculty of Science, International Islamic University Islamabad, Pakistan
[3] Department of Energy Engineering, University of the Basque Country, UPV/EHU, Nieves Cano12, Vitoria-Gasteiz 01006, Spain
[4] Department of Pharmaceutical Chemistry, College of Pharmacy, King Saud University, Riyadh 11451, Saudi Arabia

* **Correspondence:** Email: ziwen.xu@hit.edu.cn, yanhong.chen@hit.edu.cn.

Abstract: The wedge-flow configuration has particular significance in engineering applications because it provides a fundamental model for boundary-layer flow over inclined or tapered surfaces, where the imposed pressure gradient strongly influences boundary-layer development, wall shear stress, and heat transfer. Understanding and controlling these characteristics is crucial in many practical engineering applications. Existing studies, however, have mainly considered the effects of individual physical parameters, while the systematic identification of the dominant parameters governing skin-friction behavior and their subsequent use for flow prediction remains limited. Motivated by this gap, the present study aimed to analyze the flow of a non-Newtonian Eyring–Powell fluid over a wedge in the presence of magnetohydrodynamics, thermal radiation, and chemical reaction phenomena, with particular emphasis on sensitivity analysis of the flow parameters using analysis of variance to identify the dominant factors and an ANN model for rapid prediction of the flow behavior. The proposed methodology integrates numerical simulation, response surface methodology, analysis of variance-based sensitivity analysis, and a feedforward artificial neural network trained using the Levenberg–Marquardt algorithm. The magnetic field parameter was found to be the most influential factor affecting the skin friction coefficient, followed by the Eyring–Powell parameter and the wedge

parameter, according to the sensitivity analysis. The skin friction coefficient was found to range from 0.9094 to 1.1642. The ANOVA model achieved $R^2 = 100\%$, adjusted -$R^2 = 100\%$, and predicted $R^2 = 99\%$, with an overall $p < 0.005$. Moreover, the Levenberg–Marquardt artificial neural network yielded regression values ranging from 0.999 to 0.9999 and MSE values on the order of 10^{-9} for the Eyring–Powell parameters, indicating highly accurate predictions of the numerical results. The research provides useful insights into the behavior of non-Newtonian flows over wedge surfaces, as well as a practical framework for thermal-fluid analysis in high-performance aerospace, industrial, and thermal-management applications.

Keywords: Eyring–Powell fluid; magnetic field effect; thermal radiation; hybrid technique; artificial neural network; multiple-slip conditions

1. Introduction

Artificial neural networks (ANNs) are smart computational models that are meant to simulate the process of information processing by the human brain. They consist of several interconnected nodes that collaborate to identify trends, predict results, or resolve problems. ANNs are used in daily activities such as picture recognition, language translation, and recommendations, since they are independent learners. The functionality of feedforward neural networks to approximate functions is what defines its effectiveness in analyzing ordinary or partial differential equations [1]. Ahmed et al. [2] investigated the effects of thermal radiation and an inclined magnetic field on Sisko fluid flow over a radially stretching sheet. Taha et al. [3] examined the stability and dual solution of viscous fluid flow surface using machine learning and numerical simulation. Ijaz et al. [4] examined the applications of a cooling reaction using ANNs for non-Newtonian fluid flow with homogeneous/heterogeneous reaction. Zeeshan et al. [5,6] applied neural network methods to explore the wedge flow characteristics. Reddy and Das [7] examined the non-Newtonian fluid with a magnetic field over a cylinder using an ANN-based backpropagation neural network. Islam et al. [8] explored the Levenberg–Marquardt algorithm performance for Eyring–Powell fluid under magnetic force. Ali et al. [9] investigated the non-Newtonian fluid with heat transfer over a cylindrical surface using physics-informed neural network. Rehman et al. [10] explored the use of artificial intelligence for non-Newtonian fluid flow over a porous medium using numerical simulation. Several other relevant studies on non-Newtonian fluid-flow problems employing the Levenberg–Marquardt algorithm have also been reported, providing further insight into its applications and predictive capability [11,12]. Fatima et al. [13] studied heat and mass transfer over an unsteady flow using AI-based response surface methodology and the bvp4c method. Additionally, different nanofluid models incorporating various physical phenomena have been investigated using different machine-learning techniques, as discussed in [14–16].

Magnetohydrodynamics (MHD) is the study of the behavior of electrically conducting fluids in the presence of magnetic fields. Magnetohydrodynamics is a framework of study of Lorent forces, magnetic damping, and magnetic pumping, and has applications in engineering, cosmology, and industrial processes with plasma, liquid metals, and conducting liquids. Ahmed et al. [2] investigated the effects of thermal radiation and an inclined magnetic field on Sisko fluid flow over a radially stretching sheet. Jugnoo et al. [17] applied a computational method to determine the impacts of the Lorentz force and Rayleigh number on non-Newtonian fluids due to a moving surface. Recent studies have demonstrated

the significant effects of MHD on momentum and energy transport characteristics [18–20].

The effect of chemical reactions is significant in thermal condensation, batteries, rust prevention, treatment of wastewater, and biochemical processes because the rate of reaction significantly influences phenomena such as diffusion and transport. Ravikumar et al. [21] investigated non-Newtonian fluid flow in a channel under the effects of electroosmosis, Hall current, and Biot number. Zafar et al. [22] studied the Prandtl nanofluid flow across a permeable stretched surface through a Darcy–Forchheimer medium, including effects of thermal radiation and chemical reaction. ANNs have also been employed to predict the electroosmotic peristaltic flow of a Casson fluid under the effects of chemical reactions and magnetic fields [23].

The use of sensitivity analysis with analysis of variance is very useful for engineering and scientific problems because it determines the most influential factors in the system that produce a response. It facilitates parameter prioritization, optimization, process control, uncertainty reduction, and efficient decision making, rather than having to study all the parameters with the same level of importance. Samal et al. [24] conducted dominant factor analysis of the Eyring–Powell fluid model under thermal radiation and magnetic field. Bhatti et al. [25] studied the peristaltic flow of a two-phase Sisko fluid containing magnetohydrodynamics and a chemical reaction in the Darcy–Brinkman–Forchheimer porous media. Rehman et al. [26] conducted a sensitivity analysis of fluid flow over a porous surface using hybrid methodologies such as ANN and RSM. Shafique et al. [27] optimized the heat transfer of peristaltic flow across a symmetry channel using a numerical approach (bvp4c) and ANOVA-based RSM for dominant factor analysis. In previous studies, response surface methodology using the analysis of variance method has been used for sensitivity analysis and optimization of boundary layer flow and other engineering problems [28,29].

The novelty of this study lies in performing a sensitivity analysis to identify the dominant parameters influencing the skin friction coefficient and utilizing these key parameters to support effective flow control. An artificial neural network is also employed to predict flow behavior. The proposed hybrid framework integrates numerical simulation, sensitivity analysis, and ANN-based prediction to provide a comprehensive understanding of the flow system. This approach is particularly relevant to aerodynamic flow control and optimization because it identifies the most sensitive parameters and enables rapid prediction of flow behavior. Table 1 presents the research gap by comparing the present study with previous investigations and highlights the significance and novelty of the proposed work.

Table 1. Comparison with previous studies in the literature.

Factors	Ref. [3]	Ref. [13]	Ref. [19]	Ref. [24]	Ref. [30]	Present study
Dominant factor analysis	No	Yes	No	Yes	No	Yes
ANOVA-based RSM	No	Yes	No	Yes	No	Yes
ANN	Yes	Yes	No	No	No	Yes
Heat generation	No	No	Yes	Yes	No	Yes
Thermal radiation	No	No	Yes	Yes	Yes	Yes
Reaction rate	No	No	Yes	No	Yes	Yes
Heat map analysis	No	No	No	No	No	Yes

2. Problem formulation

Wedge geometries, artificial intelligence models, and sensitivity analysis have major applications across contemporary engineering systems. The wide range of applications of wedge surfaces in aerospace, turbomachinery, heat exchangers, polymer processing, civil engineering structures, and microfluidic devices includes controlling boundary-layer behavior, enhancing heat transfer, and optimizing fluid acceleration and deceleration. Artificial intelligence, particularly artificial neural networks, offers rapid and accurate predictive tools that can replace computationally intensive simulations, thereby supporting real-time monitoring, optimization, fault identification, and intelligent process control in fluid, thermal, chemical, and energy systems. Sensitivity analysis complements these tools by identifying the most influential parameters that directly affect skin friction, heat transfer, species transport, or overall system performance, thereby enabling designers to focus on the most important variables. Figure 1 illustrates the application of wedge flow in the field of aerodynamics.



Figure 1. Physical applications of the wedge flow.

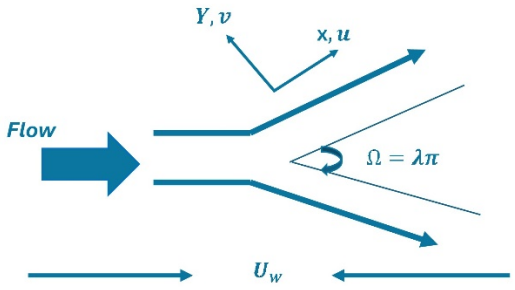


Figure 2. Flow geometry of the present work.

The present study considers a $2D$ Eyring–Powell nanofluid flow through a wedge under the influence of thermal radiation and magnetohydrodynamics. The geometrical representation of the problem is shown in Figure 2, where the velocity components are denoted by u, v along the x and y-direction. The wedge velocity is $U_w = cx^m$, and external velocity is $U_e = ax^m$, where c, a are constants, and m is the power index. A positive U_w represents a stretching surface, whereas a negative U_w corresponds to a shrinking surface. Additionally, the applied magnetic field intensity $B = B_o x^{\frac{m-1}{2}}$ is imposed normal to the surface. T_w and C_w are the surface temperature and concentration, while the ambient temperature and concentration are represented by T_∞ and C_∞, respectively. The Buongiorno nanofluid model incorporates the effect of thermophoresis and Brownian motion on nanoparticle transport.

The model represents the magnetic term as the Lorentz force, which is induced by an applied magnetic field and thus changes the fluid momentum. The thermal diffusion term in the energy equation corresponds to heat conduction. In contrast, nanoparticle transport due to random Brownian motion and temperature gradients is represented by the Brownian motion and thermophoretic terms, respectively. Energy transport mechanisms are included in the terms for thermal radiation and heat generation. The concentration equation describes the mass diffusion of nanoparticles due to Brownian motion, the thermophoretic effect, and chemical reaction. The governing equation for the Eyring–Powell fluid model is mentioned in the literature [30,31]:

Continuity equation:

$$\frac{\partial U}{\partial x} + \frac{\partial V}{\partial y} = 0. \tag{1}$$

Momentum equation:

$$u\frac{\partial U}{\partial x} + v\frac{\partial U}{\partial y} = U_e\frac{\partial U_e}{\partial x} + \left(\vartheta + \frac{1}{\rho dE}\right)\frac{\partial^2 U}{\partial y^2} - \frac{1}{2\rho dE^3}\left(\frac{\partial U}{\partial y}\right)^2\frac{\partial^2 U}{\partial y^2} + \frac{\sigma B^2}{\rho}(U_e - u). \tag{2}$$

Energy equation:

$$u\frac{\partial T}{\partial x} + v\frac{\partial T}{\partial y} = \alpha\frac{\partial^2 T}{\partial y^2} + \tau\left[D_B\frac{\partial T}{\partial y}\frac{\partial C}{\partial y} + \frac{D_T}{T_\infty}\left(\frac{\partial T}{\partial y}\right)^2\right] - \frac{1}{\rho c_f}\frac{\partial q_r}{\partial y} + \frac{Q_o(T - T_\infty)}{\rho c_f}. \tag{3}$$

Concentration equation:

$$u\frac{\partial C}{\partial x} + v\frac{\partial C}{\partial y} = D_B\frac{\partial^2 C}{\partial y^2} + \frac{D_T}{T_\infty}\frac{\partial^2 T}{\partial y^2} - k_r(C - C_\infty). \tag{4}$$

The boundary conditions are prescribed as follows [30,31]:

$$\left.\begin{aligned} U = U_w = cx^m, V = 0, -k\frac{\partial T}{\partial y} = h_f(T_w - T),\ D_B\frac{\partial C}{\partial y} = -h_s(C_w - C)\ \ at\ y = 0, \\ U \to U_e,\ \ T \to T_\infty,\ \ C \to C_\infty,\qquad at\ y \to \infty. \end{aligned}\right\} \tag{5}$$

The following similarity transformations are introduced [32]:

$$U = U_e f'(\eta) = ax^m f'(\eta), \quad V = -\sqrt{\frac{(m+1)\vartheta U_e}{2x}}\left\{f(\eta) + \left(\frac{m-1}{m+1}\right)f'(\eta).\eta\right\}, \tag{6}$$

$$\theta(\eta) = \frac{T - T_\infty}{T_w - T_\infty}, \varphi(\eta) = \frac{C - C_\infty}{C_w - C_\infty}, \eta = y\sqrt{\frac{(m+1)U_e}{2x\vartheta}}.$$

After applying the similarity transformations given in Eq (6), Eqs (2)–(4) are reduced to the following dimensionless forms:

$$(1 + K_1 - K_1K_2f''^2)f''' + \beta(1 - f'^2) + ff'' - M(2 - \beta)(f' - 1) = 0, \quad (7)$$

$$(1 + R)\theta'' + Pr[f\theta' + Nb\theta'\varphi' + Nt\theta'^2 - Q\theta] = 0, \quad (8)$$

$$\varphi'' + Scf\varphi' + \frac{Nt}{Nb}\theta'' - Cr\varphi = 0. \quad (9)$$

Also, the transformed boundary conditions are:

$$f' = \lambda,\ f = 0,\ \theta' = -Bi_1\sqrt{2-\beta}\,(1 - \theta(\eta)),\ \varphi'(\eta) = -Bi_2\sqrt{2-\beta}\,(1 - \varphi(\eta)),\ at\ \eta = 0,$$

$$f' \to 1,\ \theta \to 0,\ \varphi \to 0,\ \ at\ \eta \to \infty. \quad (10)$$

The dimensionless parameters after the simulation are defined as:

$$K_1 = \frac{1}{\mu Ed}, \beta = \frac{2m}{m+1},\ M = \frac{2\sigma B_0^2}{\rho a}, K_2 = \frac{U_e^3(m+1)}{2\vartheta xE^2}, \lambda = \frac{c}{a}\ Pr = \frac{\vartheta}{\alpha}, Nb = \frac{\tau D_B(C_w - C_\infty)}{\vartheta},\ Q = \frac{Q_o}{\rho c_f a},$$

$$Nt = \frac{\tau D_T(T_w - T_\infty)}{T_\infty \vartheta},\ Sc = \frac{\vartheta}{D_B}, Bi_1 = -\frac{h_f}{k}\sqrt{\frac{\vartheta}{a}}, R = \frac{16\sigma^* T_\infty^3}{3k^*k_1^*}, Bi_2 = -\frac{h_s}{D_B}\sqrt{\frac{\vartheta}{a}}, Cr = \frac{2k_r x}{U_e(m+1)}.$$

The engineering physical quantities of interest [28,29] are defined as:

$$Cf_xRe^{\frac{1}{2}} = (1 + K_1)f''(0) - \frac{K_1K_2}{3}f''^3(0),\ \sqrt{2-\beta}\,Nu_xRe^{-\frac{1}{2}} = -(1 + R)\theta'(0). \quad (11)$$

3. Methodology

In this study, a hybrid approach incorporating numerical simulation, statistical sensitivity analysis, and artificial neural network prediction is employed to investigate the flow, heat transfer, and mass transfer characteristics of an Eyring–Powell non-Newtonian fluid over a wedge under the combined effects of a magnetic field, thermal radiation, and chemical reaction. The three complementary components of this approach ensure the accuracy of the physically based results, identify the relative importance of the governing parameters, and facilitate the development of a rapid predictive model that can serve as an alternative to the numerical solver.

3.1. Numerical solution and computational implementation

The initial step involves formulating and solving the nonlinear differential equations that describe the velocity, temperature, and concentration fields. The mathematical model is formulated using the continuity, momentum, energy, and species concentration equations, incorporating the effects of Eyring–Powell rheology, magnetic field, heat generation, thermal radiation, and chemical reaction. Similarity transformations are used to transform the partial differential equations into a coupled system

of ordinary differential equations. The transformed equations are numerically solved using MATLAB's BVP4C solver, a robust boundary-value problem solver based on a collocation method with residual control. The solver iteratively adjusts the initial solution guess to satisfy the prescribed boundary conditions, including those imposed at the truncated far-field boundary. Mesh refinement is performed to ensure grid independence, and appropriate convergence criteria are applied to verify the reliability of the solutions. The numerical results provide detailed profiles of velocity, temperature, and concentration for different parameter values. Furthermore, important engineering performance quantities, including the skin friction coefficient, Nusselt number, and Sherwood number, are calculated from the numerical solutions and used as the basis for further analysis. For computational implementation, the following new variables are introduced:

$$f = y_1\,, f' = y_2, f'' = y_3,\ f''' = y_3', \theta(\eta) = y(4), \theta'(\eta) = y(5),$$

$$\theta''(\eta) = y_5',\ \varphi(\eta) = y_6,\ \varphi'(\eta) = y_7,\ \varphi''(\eta) = y'_7\,. \tag{12}$$

For the implementation of the boundary conditions, the subscripts a and b denote the values at $\eta = 0$ and $\eta \to \infty$, respectively. Thus, $y_a(1)$ represents $f(\eta)$ at $\eta = 0$.

$$dydx=[y(2); y(3); \frac{(M*(y(2)-1)*(2-\beta))-y(1)*y(3)+\beta*\left(\left(y(2)\right)^2\right)-1\right)}{(1+K1-K1*K2*((y(3))\text{^}2))}; \tag{13}$$

$$y(5); -\frac{Pr*y(1)*y(5)+Pr*Nt*\left(\left(y(5)\right)^2\right)+Pr*Nb*y(5)*y(7)+Pr*Q*y(4)}{(1+R)}; \tag{14}$$

$$y(7);\ -(\frac{Nt}{Nb}) * (-(Pr * y(1) * y(5) + Pr * Nt * ((y(5))^2) + Pr * Nb * y(5) * y(7) + Pr * Q * y(4))/(1 + R)) - Sc * y(1) * y(7) + Sc * y(7) * Cr;] \tag{15}$$

$$ya(1);\quad ya(2) - \lambda;\ ya(5) + Bi1 * (2 - \beta) * \left(1 - ya(4)\right);\ ya(7) + Bi2 * (2 - \beta) * \left(1 - ya(6)\right);\quad yb(2) - 1;\ yb(4);\ yb(6). \tag{16}$$

3.2. Sensitivity analysis using analysis of variance

The parameters influencing the skin friction coefficient were selected based on their physical significance and their roles in the mathematical model. These parameters include the Eyring–Powell fluid parameter, magnetic parameter, stretching/shrinking parameter, wedge-angle parameter, Biot number, and chemical reaction parameter.

Step 1: The lower and upper values of each selected parameter were defined according to the physical range considered in the investigation. These ranges were then used as the domain for the statistical analysis.

Step 2: Numerical solutions of the governing equations were obtained for the selected combinations of input parameters, and the corresponding skin friction coefficient was calculated. These numerical results were used as the response data for the response surface methodology analysis. The numerical experiments were designed using response surface methodology to determine the relationship between the selected input parameters and the skin friction coefficient. This approach not only reduces the number of numerical simulations required but also provides sufficient information

about the individual and combined effects of the parameters.

Step 3: The numerical results were used to develop a response surface regression equation. The regression model describes the variation in the skin friction coefficient with respect to the selected parameters and their interaction effects.

Step 4: The developed regression model and the individual parameters were analyzed for statistical significance using analysis of variance. The F-value and p-value were used to determine whether each factor had a significant effect on the skin friction coefficient. A p-value < 0.05 was considered statistically significant.

Step 5: The effects of the parameters were evaluated using the analysis of variance and Pareto analyses. This step identifies the most significant parameters influencing variations in the skin friction coefficient and provides a quantitative basis for ranking the parameters according to their sensitivity.

Step 6: Diagnostic plots were used to evaluate the adequacy of the regression model. The normality of the residuals was assessed using a normal probability plot, while the independence and randomness of the residuals were examined using the residuals-versus-run plot.

Step 7: The performance of the response surface methodology model was evaluated using statistical measures, including R^2, adjusted R^2, predicted R^2, and overall model significance. These measures indicate how well the regression model fits the numerical data and reflects its predictive capability.

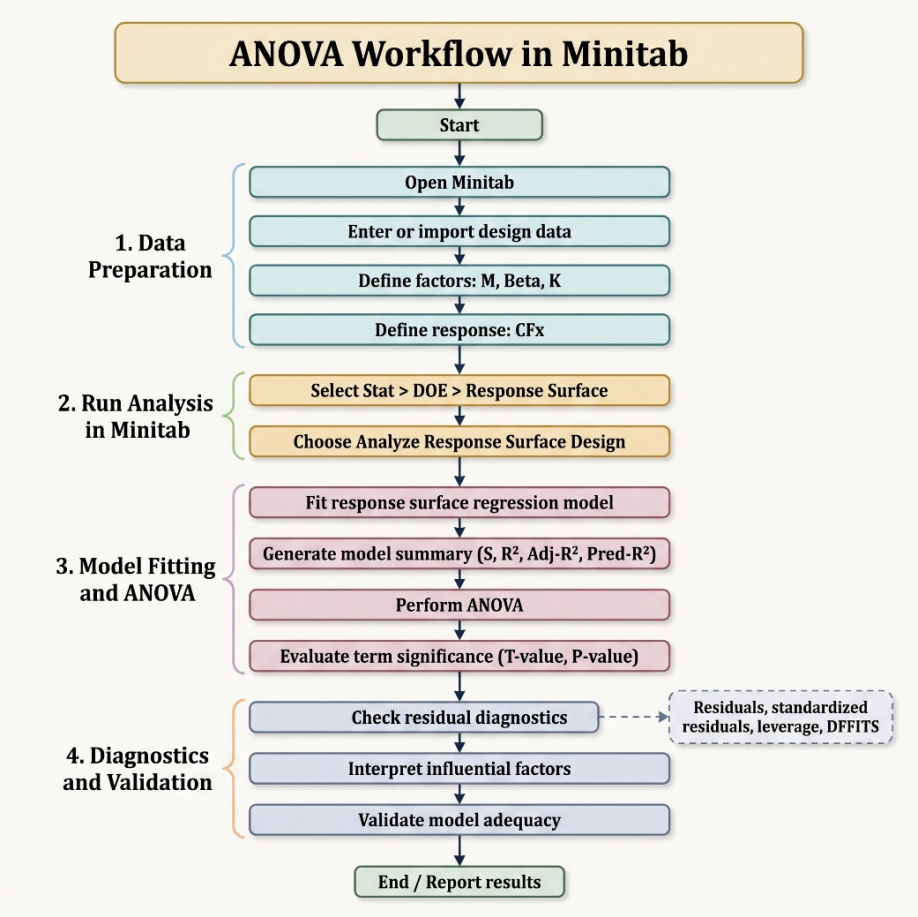


Figure 3. Workflow of ANOVA-based sensitivity analysis.

The critical parameters identified in this analysis can help control the skin friction coefficient and may therefore be useful for aerodynamic flow control, drag reduction, and the optimization of wedge-type flow systems. Figure 3 illustrates the variance-based response surface methodology procedure used for sensitivity analysis. The sensitivity equation for the skin friction coefficient is given as follows:

$$\mathrm{C}f\mathrm{x} = 7478.97 + 643A + 287.54B - 454.76C - 17.65A^2 + 26.33C^2 - 39.17AB - 18.18AC - 8.21BC \quad (17)$$

3.3. Prediction and analysis using an artificial neural network (ANN)

The third step is devoted to the creation of an artificial neural network model that would predict fluid behavior in a rather short time, as an effective surrogate of the numerical solver. The magnetic field parameter M and chemical reaction parameter Cr are the inputs in the numerical dataset, and the feedforward neural network is trained on the numerical data. The results are velocity, temperature, and concentration profiles, skin friction coefficient, heat transfer, and mass transfer. The Levenberg–Marquardt training algorithm was chosen because it is faster and more reliable for nonlinear regression issues. To avoid overfitting, the dataset is split into training (70%), validation (15%), and testing (15%). A feedforward neural network is used to predict the flow response. The ANN has four input variables, 15 neurons in the hidden layer, and one output variable. Four input parameters are fed to the input layer, and the selected flow quantity is taken as the output. Optimization of the network weights and biases is done by the Levenberg–Marquardt algorithm. The mean squared error is used as the performance function to evaluate the difference between the numerical and ANN-predicted values. Error histograms are used to see the distribution of errors in prediction, MSE curves are used to see the learning progress over epochs, and regression plots are used to see the linearity between ANN outputs and the target numerical values. The gradient reduction and the behavior of the Levenberg–Marquardt parameter are illustrated by training graphs. ANN attains very small values of mean-squared error around R and with correlation coefficients $R = 0.999$. These findings demonstrate that the ANN model is effective in reproducing numerical solutions with minimum error. After training, the ANN can make predictions regarding flow, thermal, and concentration behavior of new parameters virtually in real time; thus, it is well-suited to optimization, control, and real-time uses.

4. Results and discussion

The results section is divided into three parts, presenting the results obtained from the numerical simulation, artificial neural network analysis, and response surface methodology. Table 2 presents the thermophysical values of the parameters used in the simulations of the present problem. Table 3 presents the values of input parameters with their lower, central, and upper value in response surface methodology, and Table 4 shows the result of the skin friction coefficient for value selection in analysis of variance. Table 5 shows regression and prediction results, in which $p < 0.05$ is considered significant. Table 6 shows the results of the analysis of variance: linear model, lack of fit, and error. Table 7 shows the results of the artificial neural network: epoch, MSE, regression, and Mu.

Table 2. Range of thermophysical parameters.

K_1	K_2	$\lambda = R = Q$	$\beta = M$	Bi_1	Nt	Nb	Cr
0.1	0.1	0.2	0.5	0.1	0.4	0.3	0.7
0.4							
0.7							
	0.1	0.2	0.5	0.1	0.4	0.3	0.7
	0.9						
	1.8						
		0.1	0.5	0.1	0.4	0.3	0.7
		0.2					
		0.3					
			0.1	0.1	0.4	0.3	0.7
			0.5				
			0.9				
				0.1	0.4	0.3	0.7
				0.15			
				0.2			
					0.1	0.3	0.7
					0.4		
					0.7		
						0.3	0.7
						0.5	
						0.7	
							0.5
							0.6
							0.7

Table 3. Selecting input levels for CCD.

Factor	Coded symbol	Levels		
		Lower	Middle	Upper
M	A	0.5	0.6	0.7
β	B	0.1	0.2	0.3
$K_1 = K$	C	0.1	0.2	0.3

Table 4. Response of the skin-friction coefficient.

Experiment	M	β	K	Cf_x
1	0.7	0.3	0.1	1.1642
2	0.6	0.2	0.2	1.0379
3	0.5	0.3	0.3	0.9697
4	0.6	0.2	0.368179	0.9738
5	0.431821	0.2	0.2	0.9339

Continued on next page

Experiment	M	β	K	Cf_x
6	0.768179	0.2	0.2	1.133
7	0.5	0.1	0.1	0.9861
8	0.5	0.3	0.1	1.0511
9	0.7	0.3	0.3	1.0748
10	0.6	0.2	0.2	1.0379
11	0.6	0.2	0.2	1.0379
12	0.6	0.031821	0.2	0.9928
13	0.6	0.2	0.2	1.0379
14	0.6	0.2	0.2	1.0379
15	0.6	0.368179	0.2	1.0812
16	0.6	0.2	0.031821	1.1154
17	0.5	0.1	0.3	0.9094
18	0.6	0.2	0.2	1.0379
19	0.7	0.1	0.1	1.1188
20	0.7	0.1	0.3	1.0326

Table 5. Regression and prediction results.

Term	T-value	P-value	
Constant	7478.97	0.000	Significant
M	643.32	0.000	Significant
Beta	287.54	0.000	Significant
K	-454.76	0.000	Significant
$M * M$	-17.65	0.000	Significant
Beta∗Beta	-3.64	0.005	Not Significant
$K * K$	26.33	0.000	Significant
M ∗Beta	-39.17	0.000	Significant
$M * K$	-18.18	0.000	Significant
Beta $* K$	-8.21	0.000	Significant
	$\boldsymbol{R^2 = 100\%}$	$\boldsymbol{Adj - R^2 = 100\%}$	$\boldsymbol{Pred - R^2 = 99\%}$

Table 6. Analysis of variance.

Source	DF	Adj SS	Adj MS	F-value	P-value
Model	9	0.081788	0.009088	78,490.32	0.000
Linear	3	0.081434	0.027145	234,450.76	0.000
Square	3	0.000131	0.000044	376.03	0.000
2-way interaction	3	0.000224	0.000075	644.17	0.000
Error	10	0.000001	0.000000		
Lack-of-fit	5	0.000001	0.000000	*	*
Pure error	5	0.000000	0.000000		
Total	19	0.081789			

Table 7. Artificial neural network response.

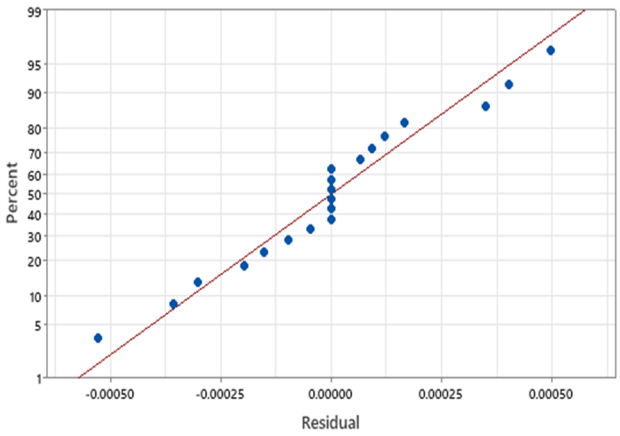
Scenarios	MSE			Performance	Gradient	Mu	Epoch
	Training	Validation	Testing				
$S_1 = K_1$	9.6158e-10	1.05377e-9	1.11108e-9	9.09e-10	2.80e-7	1e-11	77
$S_2 = K_2$	8.9145e-10	1.05936e-9	1.12231e-9	8.91e-10	9.83e-8	1e-11	126
$S_3 = R$	4.25844e-5	4.06925e-5	3.76307e-5	4.25e-5	8.75e-7	1e-8	50
$S_4 = Cr$	1.97352e-4	1.94272e-4	1.79610e-4	0.000197	4.27e-5	1e-6	12

4.1. Sensitivity analysis of the skin friction coefficient

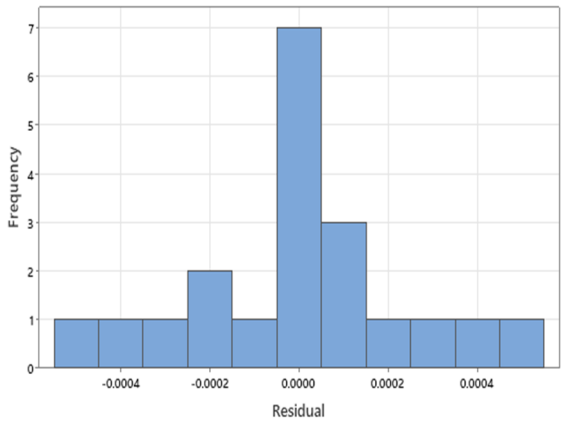
In this section, the results obtained using response surface methodology (RSM), including probability plots, observation-order plots, and residual plots, are discussed. The fact that the statistical model and the experimental design are sound and physically meaningful is supported by the sensitivity analysis of the skin friction coefficient $(\mathrm{C}f\mathrm{x})$ based on response surface methodology that relies on analysis of variance.

The normal probability plot shown in Figure 4(a) indicates the presence of residuals that are clustered around the straight line, which implies that the unexplained errors are not associated with a trend or not well governed by physics, but are associated with noise; this is supported by the fact that the histogram in Figure 4(b) is almost symmetric and bell-shaped, indicating no strong skewness or outliers that would influence the estimates of $\mathrm{C}f\mathrm{x}$. The difference between the residual values and those in Figure 4(c) shows no systematic change over time, indicating random variance; therefore, time-related effects (such as equipment warming, operator learning, or unknown environmental changes) are not observed, and hence, the assumption of independence in analysis of variance is met. Factor A has the largest standardized effect in the Pareto chart shown in Figure 4(d), followed by factor B and some interaction terms, implying that shifts in factor A and B have relatively large effects on $\mathrm{C}f\mathrm{x}$. Their t-statistics are statistically significant above the reference line; thus, they are significant rather than mere numerical noise. Physically, this means that mechanisms represented by A and B (e.g., Reynolds number, surface roughness, or thermal parameter, depending on the definition) have the most significant control over the momentum transfer at the wall.

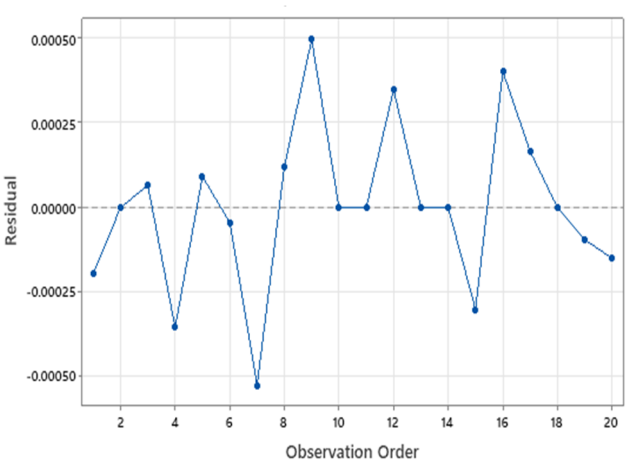
In contrast, other mechanisms have lesser or insignificant control under the ranges of operation testing. These relationships are illustrated in Figure 4(e); strong positive correlations imply that an increase in a particular factor leads to an increase in $\mathrm{C}f\mathrm{x}$, and strong negative correlations imply that an increase in a particular factor causes a decrease in $\mathrm{C}f\mathrm{x}$; these can be used to understand how combinations of parameters can reinforce or overcome one another. Lastly, the fitted regression plot shown in Figure 4(f) indicates that the predicted values of the RSM model result in the experimentally observed points with reasonably small confidence bands, indicating that the selected form of a polymer and the interactions that were added are adequate to capture the observed behavior without overfitting. Collectively, these diagnostic graphs indicate that the models are statistically good, the physics that prevail are represented by factors A and B and their interactions, and $\mathrm{C}f\mathrm{x}$ is the most responsive to manipulations in these key parameters, so they are the main levers for design and optimization.



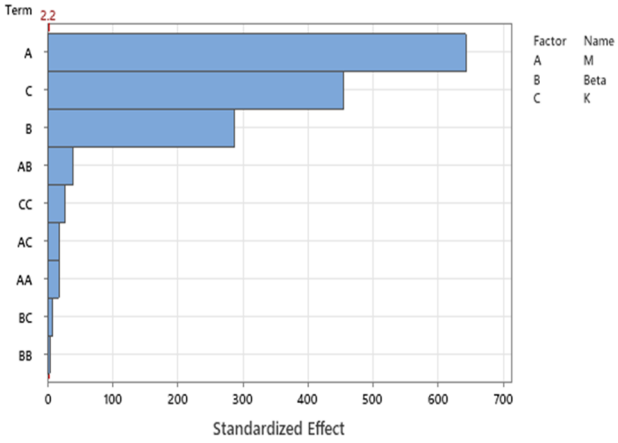
(a) Normal probability plot for Cfx.



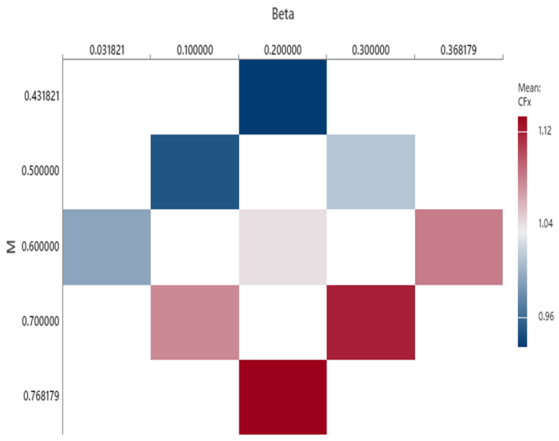
(b) Histogram of residuals for Cfx.



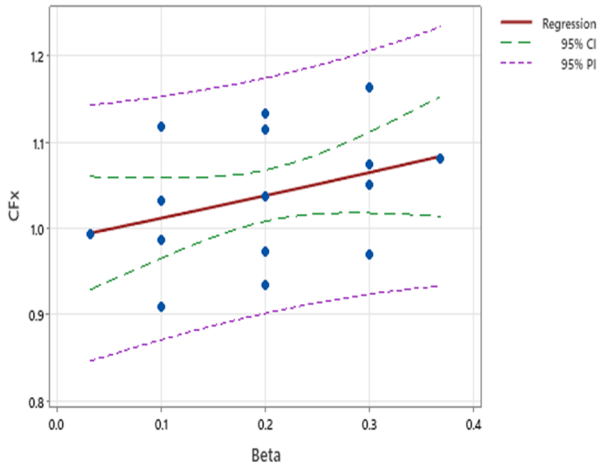
(c) Observation-order plot for Cfx.



(d) Pareto chart plot for Cfx.



(e) Heatmap plot for Cfx.

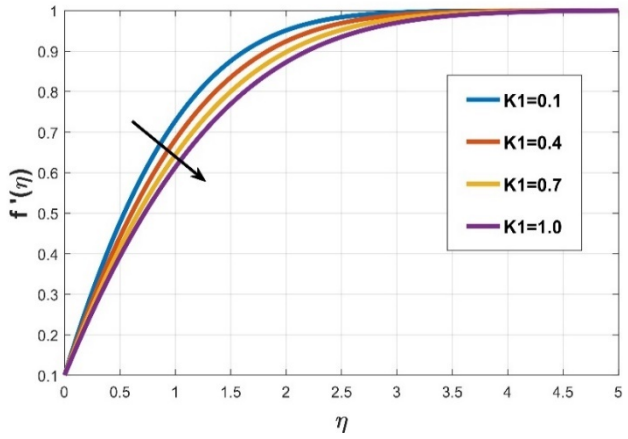


(f) Regression plot for Cfx.

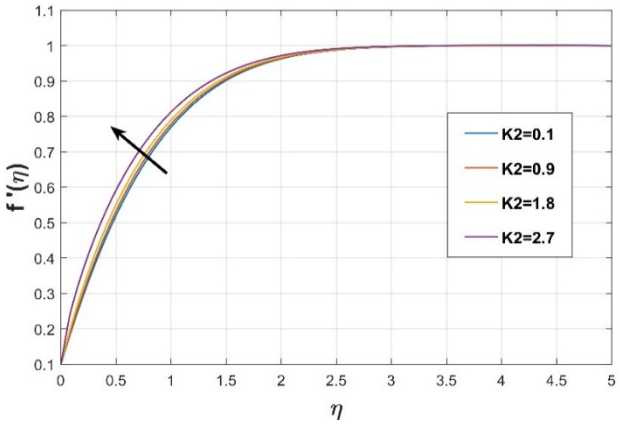
Figure 4. Statistical diagnostics and sensitivity analysis of the skin friction coefficient (Cfx) using response surface methodology (RSM).

4.2. Flow behavior profiles

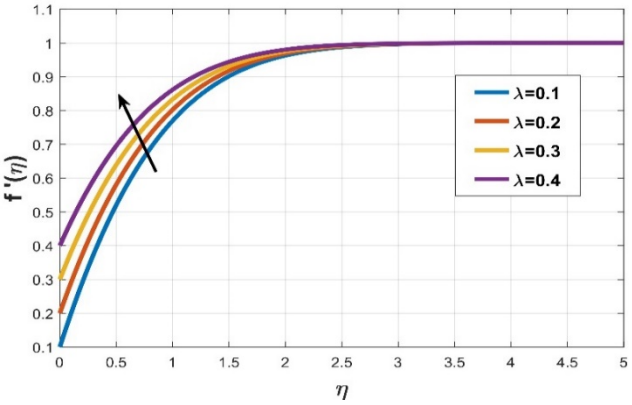
In this section, the effects of various physical parameters, including the Eyring–Powell fluid parameter, magnetic parameter, thermal radiation parameter, chemical reaction parameter, wedge parameter, and slip boundary condition, on flow behavior are discussed.



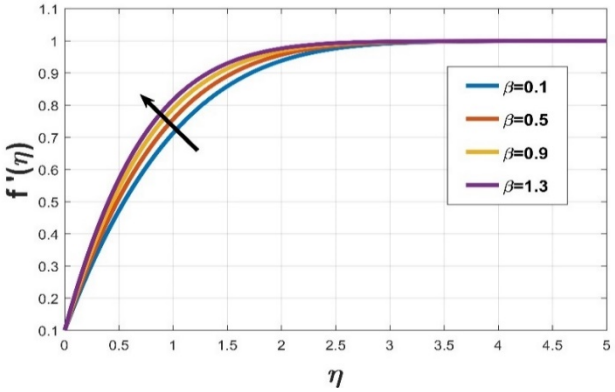
(a) Impact of $\boldsymbol{K_1}$ on velocity profile.



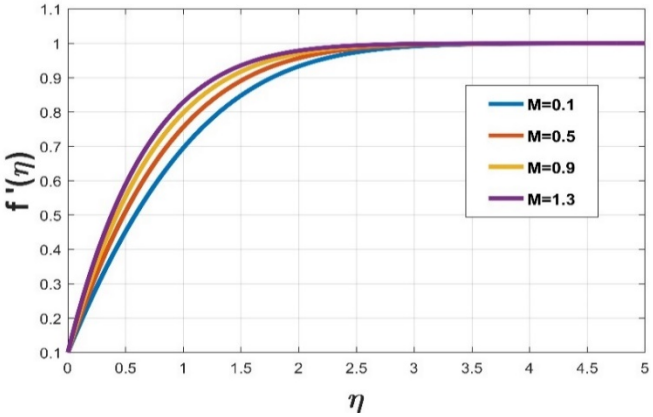
(b) Impact of $\boldsymbol{K_2}$ on velocity profile.



(c) Impact of $\boldsymbol{\lambda}$ on velocity profile.

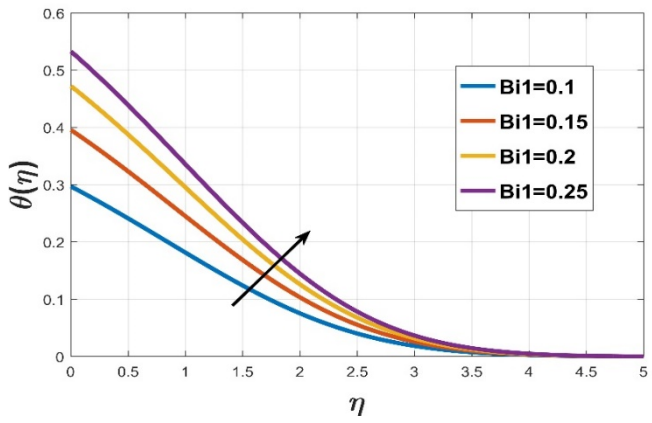


(d) Impact of $\boldsymbol{\beta}$ on velocity profile.

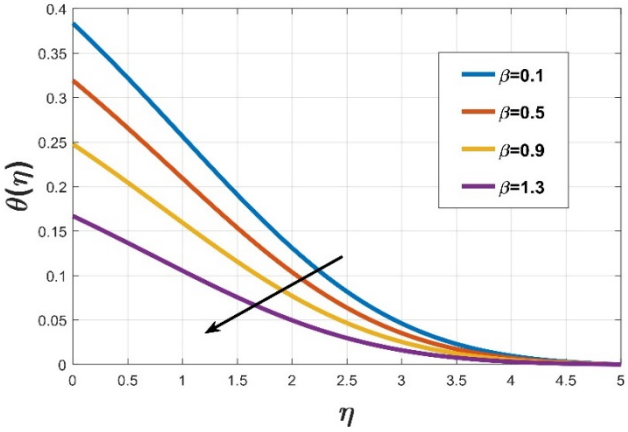


(e) Impact of $\boldsymbol{M}$ on velocity profile.

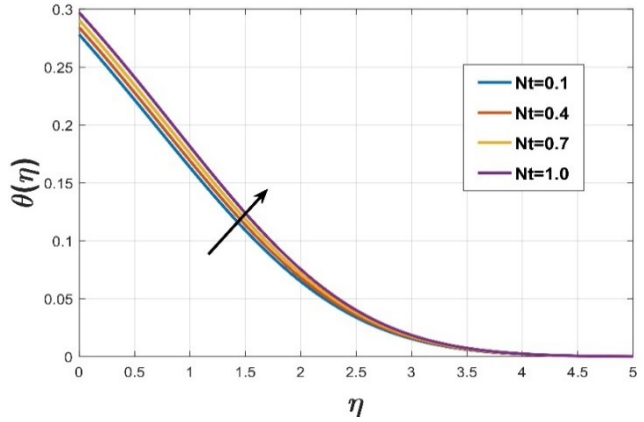
Figure 5. Effects of various physical parameters on the velocity profile $(f'(\eta))$.



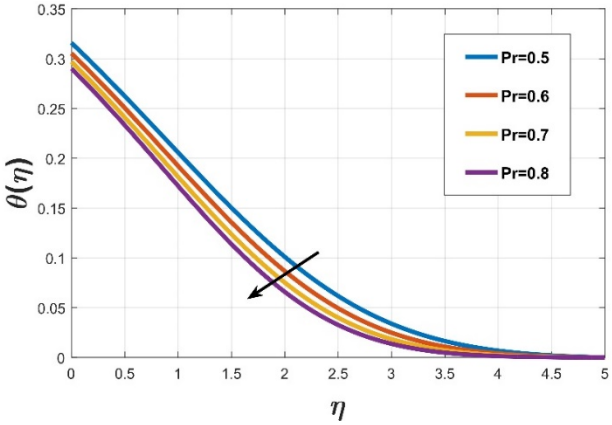
(a) Impact of $\boldsymbol{Bi_1}$ on energy profile.



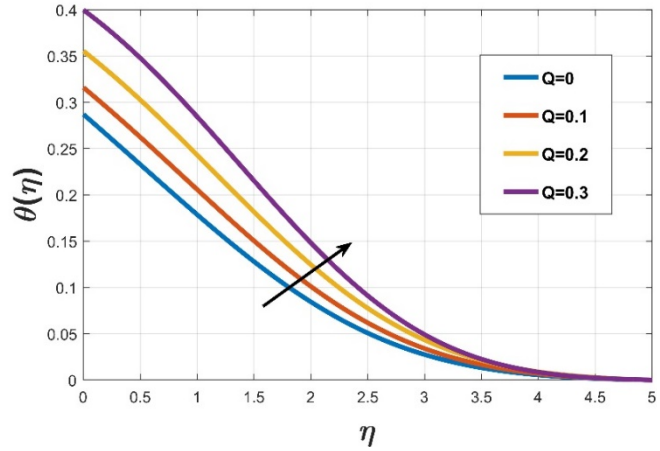
(b) Impact of $\boldsymbol{\beta}$ on energy profile.



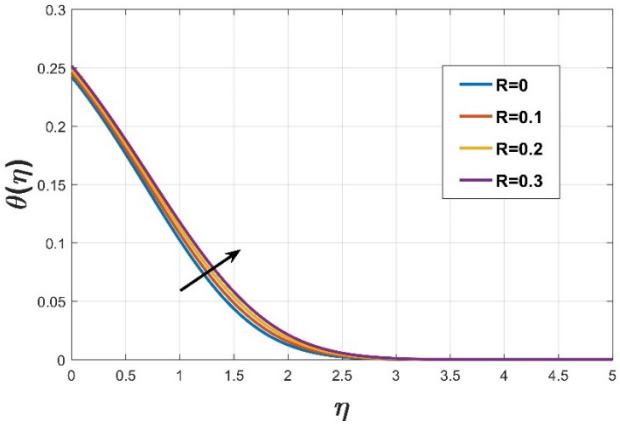
(c) Impact of $\boldsymbol{Nt}$ on energy profile.



(d) Impact of $\boldsymbol{Pr}$ on energy profile.

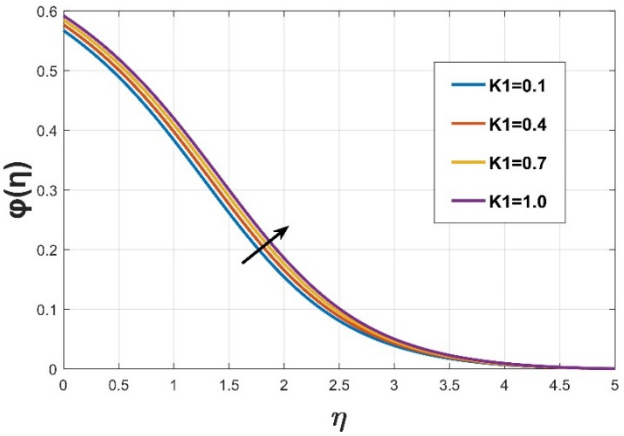


(e) Impact of $\boldsymbol{Q}$ on energy profile.

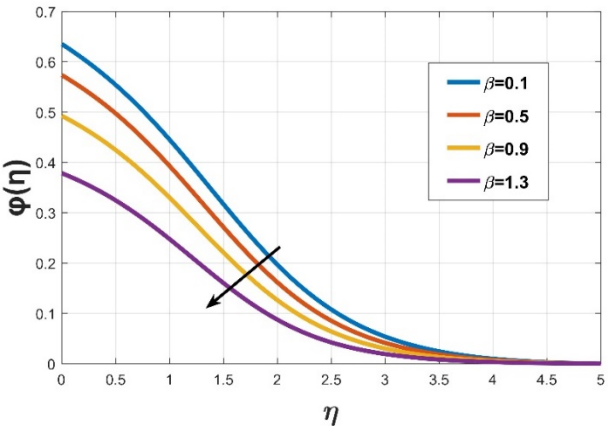


(f) Impact of $\boldsymbol{R}$ on energy profile.

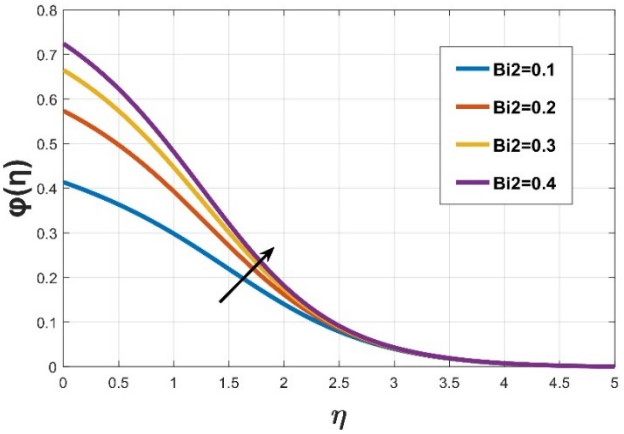
Figure 6. Effects of various physical parameters on the temperature profile $(\theta(\eta))$.



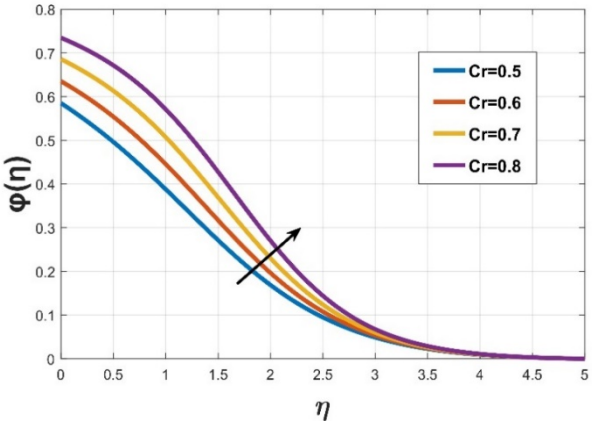
(a) Impact of $\boldsymbol{K_1}$ on concentration profile.



(b) Impact of $\boldsymbol{\beta}$ on concentration profile.



(c) Impact of $\boldsymbol{Bi_2}$ on concentration profile.



(d) Impact of $\boldsymbol{Cr}$ on concentration profile.

Figure 7. Effects of various physical parameters on the concentration profile $(\varphi(\eta))$.

Figure 5(a)–(e) shows the impact of various parameters on the velocity profile, such as the magnetic field parameter, Eyring–Powell fluid parameter, and wedge angle parameter. Figure 5(a) shows that the velocity profile decreases with an increase in the Eyring–Powell parameter (K_1). An increase in K_1 strengthens the non-Newtonian effects and enhances the resistance to fluid motion, thereby reducing the fluid velocity near the surface. Conversely, Figure 5(b) indicates that the velocity profile increases with an increase in the Eyring–Powell fluid parameter (K_2); here, the term K_2 decreases the effective viscous resistance, thus resulting in an accelerating fluid and a thinner momentum boundary layer. Figure 5(c) shows that the velocity profile increases with the stretching/shrinking parameter. A stiffer stretch pushes more fluid across the surface, and the fluid momentum is larger, resulting in a higher velocity profile. As seen in Figure 5(d), the velocity profile increases with increasing wedge angle parameter (β). Due to the increased flow passage, the flow resistance decreases, and the fluid is accelerated along the surface of the wedge, causing the velocity profile to increase. Figure 5(e) shows that the magnetic parameter (M) increases with velocity for the present configuration. This rise is due to the Lorentz force provided by the magnetic field applied in the direction of the flow, which helps the momentum of the fluid, thus accelerating it. The behavior of the temperature (energy) profile is described in Figure 6(a)–(f). Figure 6(a) shows that the temperature

profile rises with the thermal Biot number (Bi_1). A greater Biot number (Bi_1) indicates greater convective heating at the surface, injecting more energy into the fluid and making the thermal boundary layer thicker. Figure 6(b) indicates that an increase in the wedge angle parameter (β) decreases the temperature profile: the quicker flow with the larger value of β increases convective cooling and thus lowers the fluid temperature near the wall. As shown in Figure 6(c), the temperature profile increases with an increase in the thermophoresis parameter (Nt). This behavior is attributed to the higher thermophoretic effect, which causes nanoparticles to be transported from the hotter zone to the colder zone; hence, the higher transport of nanoparticles further leads to higher heat accumulation in the thermal boundary layer.

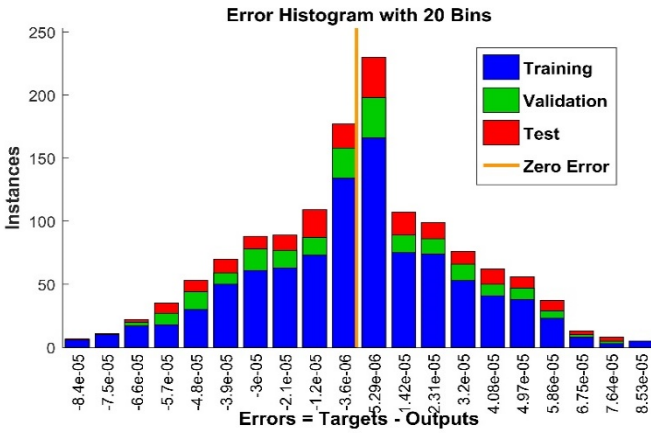
Figure 6(d) illustrates that the higher the Prandtl number (Pr), the lower the temperature. Because an increased Prandtl number (Pr) results in an increased momentum diffusivity over thermal diffusivity, heat diffuses more gradually, and the thermal boundary layer is reduced, providing a reduced temperature field. The temperature profile is improved by increasing the heat generation parameter (Q) and thermal radiation parameter (R), as demonstrated in Figure 6(e),(f). An increase in the heat-generation parameter supplies additional thermal energy to the fluid, thereby raising its temperature. Similarly, an increase in the thermal radiation parameter enhances radiative energy transfer within the boundary layer, resulting in a higher temperature. Consequently, in both cases, the temperature decreases more gradually away from the surface.

The variation in concentration profile is given in Figure 7(a)–(d). Figure 7(a) shows that the more pronounced the non-Newtonian effect that decelerates the fluid, the higher the Eyring–Powell parameter (K_1) the higher the concentration profile, which means that the species is convectively transported away from the wall, and the higher concentration remains close to the surface. Figure 7(b) indicates that as the wedge angle parameter is raised, the concentration level goes down; the higher the velocity of the fluid movement in relation to β, the more the mass is convected, and hence, the species is diffused away more rapidly, and the concentration boundary layer becomes smaller. Figure 7(c) depicts that the higher the mass Biot number, the greater the concentration profile, since the higher the convective mass transfer at the surface, the more the fluid provides species to the fluid, and the boundary layer of concentration becomes thicker. Figure 7(d) shows that the higher the chemical reaction parameter (Cr), the higher the concentration profile rises, meaning that the overall effect of the reaction in this model is to produce or maintain more species in the fluid, resulting in higher levels of concentration across the entire boundary layer.

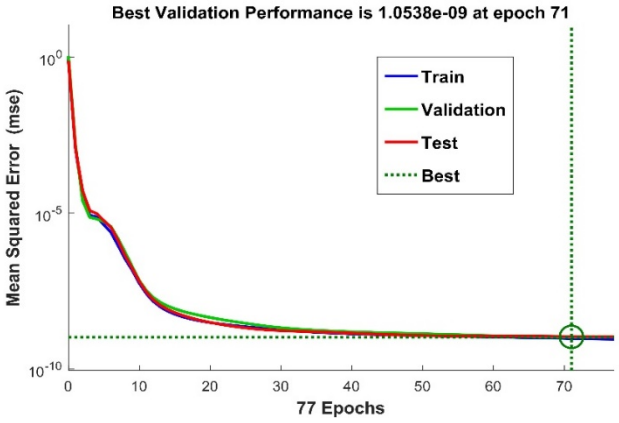
4.3. Feedforward neural network analysis

The predictive performance of the various factors is analyzed using a feedforward neural network in terms of the regression coefficient (R), number of iterations, and mean squared error (MSE).

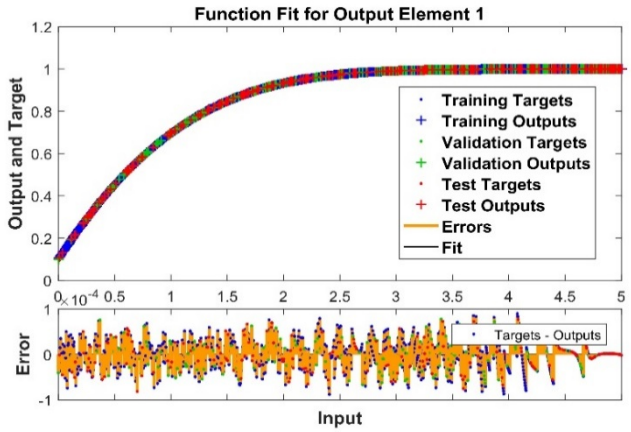
For the Eyring–Powell fluid parameter K_1, the neural network exhibited highly accurate learning behavior. In Figure 8(a), the error distribution is strongly concentrated around the value 0. The mean squared error (MSE) curve in Figure 8(b) indicates rapid convergence, reaching an optimum validation error at epoch 71 with an extremely small MSE of $1.1 * 10^{-9}$. The close agreement between the predicted and actual values in Figure 8(c), as well as the regression coefficient of $R \approx 0.9999$ in Figure 8(d), demonstrates that the ANN can accurately capture the effect. Figure 8(e) shows that the gradient gradually reduces to $2.79 * 10^{-7}$ to achieve its training performance.



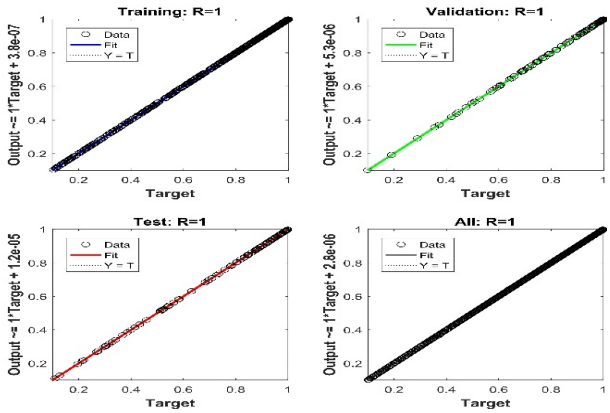
(a) Error bar plot for K_1.



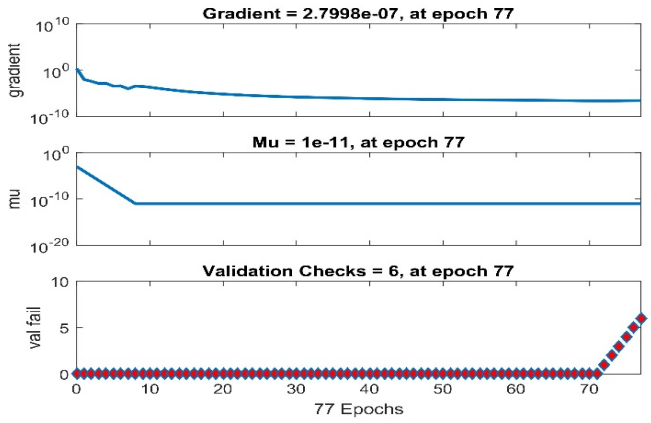
(b) MSE plot for K_1.



(c) Fitness function plot for K_1.

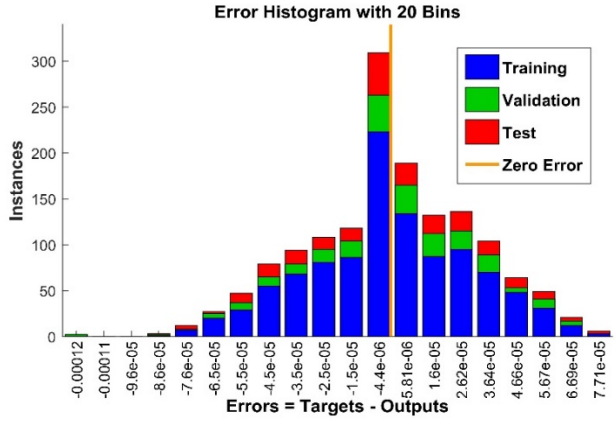


(d) Regression plot for K_1.

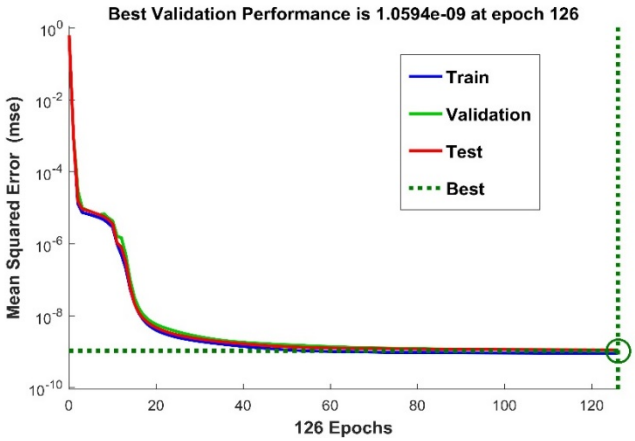


(e) Training plot for K_1.

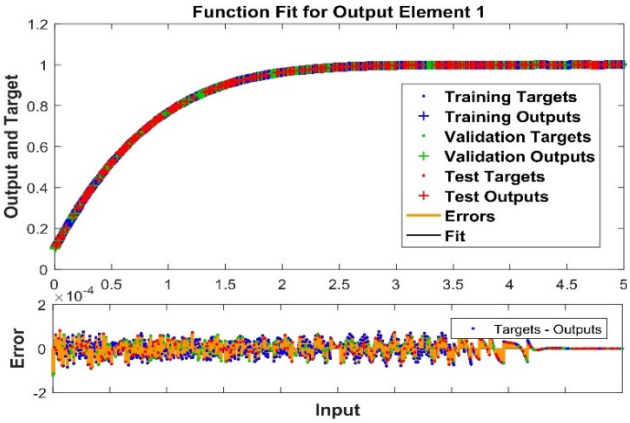
Figure 8. Artificial neural network performance evaluation for (K_1): (a) error histogram, (b) mean squared error (MSE), (c) fitness function, (d) regression analysis, and (e) training performance.



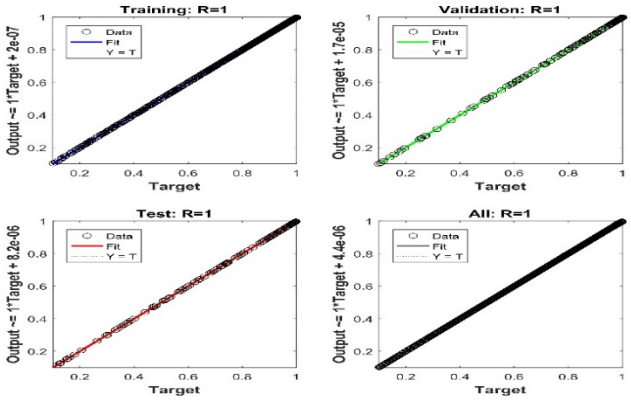
(a) Error bar plot for K_2.



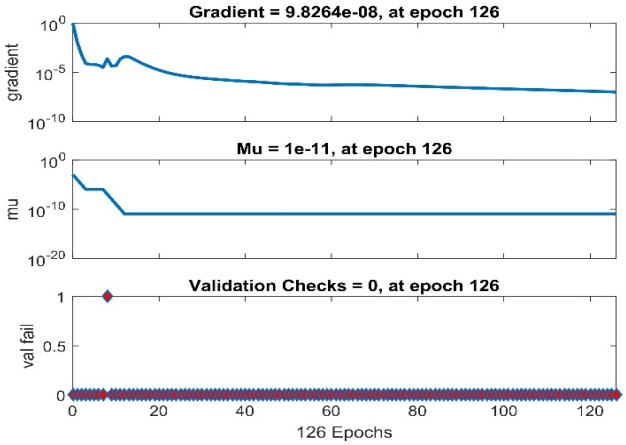
(b) MSE plot for K_2.



(c) Fitness function plot for K_2.

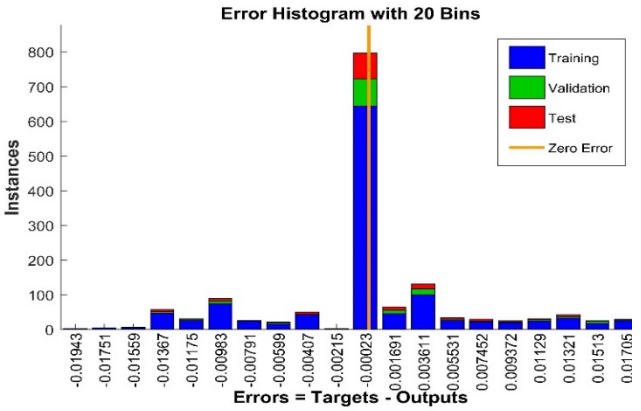


(d) Regression plot for K_2.

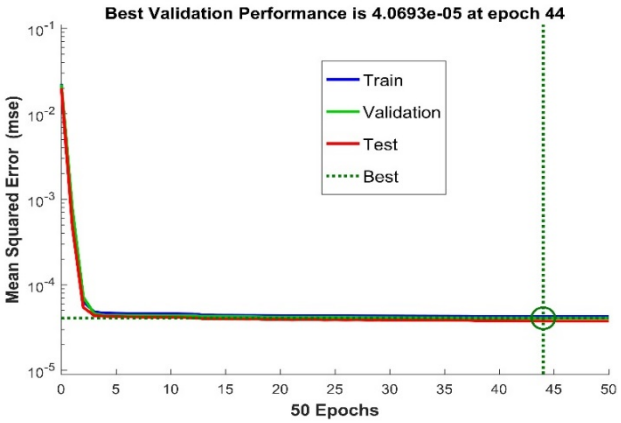


(e) Training plot for K_2.

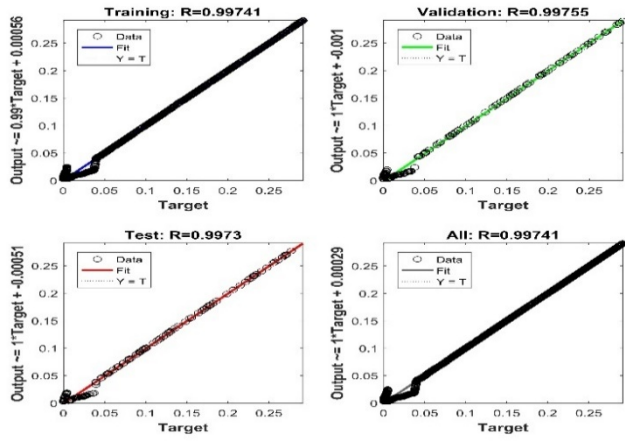
Figure 9. Artificial neural network performance evaluation for (K_2): (a) error histogram, (b) mean squared error (MSE), (c) fitness function, (d) regression analysis, and (e) training performance.



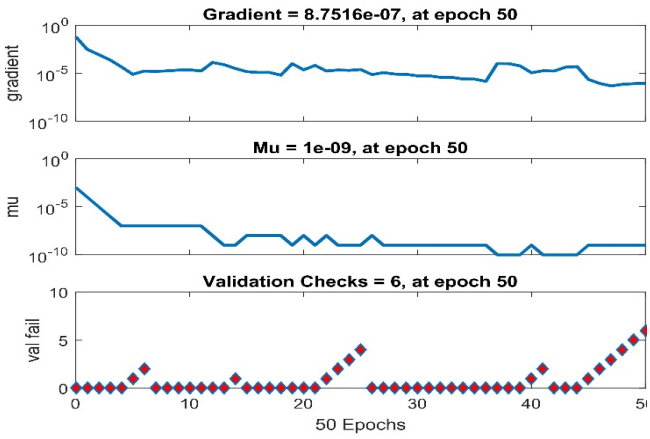
(a)Error bar plot for R.



(b) MSE plot for R.



(c) Regression plot for R.



(d) Training plot for R.

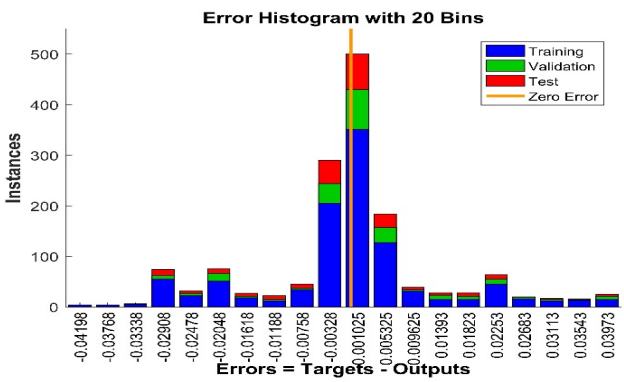
Figure 10. Artificial neural network performance evaluation for (R): (a) error histogram, (b) mean squared error (MSE), (c) regression analysis, and (d) training performance.

These results confirm the stable and effective convergence of the Levenberg–Marquardt (LM) algorithm. For the Eyring–Powell parameter K_2, the same accuracy is preserved. Figure 9(a) indicates a steep concentration error at zero, and Figure 9(b) indicates that the curve of MSE is at its most optimal at epoch 126 with an MSE of $1.7 * 10^{-9}$. The almost flawless curve in Figure 9(c) and the accuracy of the regression at $R \approx 0.9999$ in Figure 9(d) all validate that the ANN is effectively approximating the behavior of K_2. Figure 9(e) presents a gradient decreasing to $9.82 * 10^{-8}$, which is the training performance with smooth convergence.

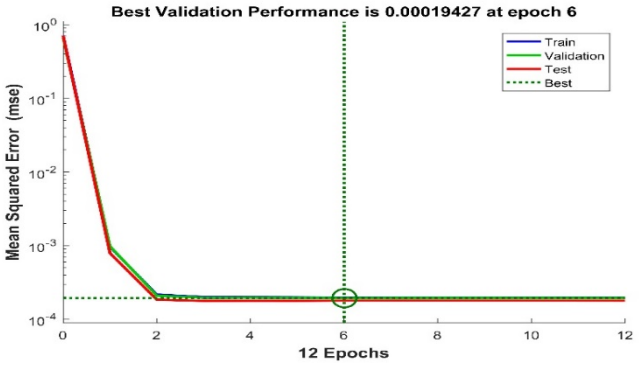
Regarding the third scenario, which considers thermal radiation R, the neural network once again presents high predictive ability, but with a small additional error since temperature fields driven by thermal radiation are highly sensitive. Figure 10(a) reveals that the maximum error is at zero, and Figure 10(b) reveals that the optimal MSE is at epoch 44. In the regression plot of Figure 10(c), the high correlation of about 0.999 demonstrates that the ANN follows the actual temperature profile response. Figure 10(d) indicates that the training plot is stable with the gradient smoothly reduced and

the Levenberg–Marquardt parameter controlled, thus validating effective convergence of this case.

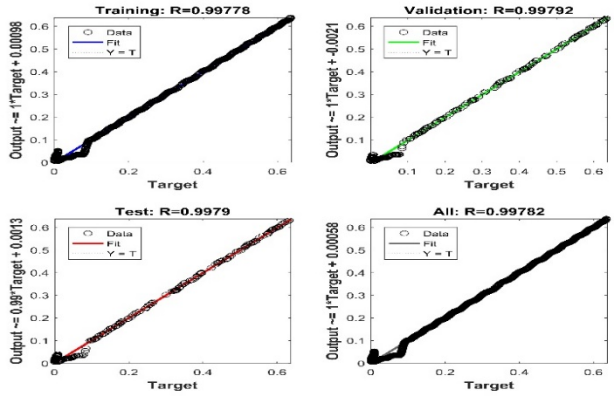
Finally, for the fourth scenario, when the chemical reaction parameter is considered, the ANN once again works with high accuracy. The error histogram in Figure 11(a) is concentrated sharply around zero, and the MSE curve in Figure 11(b) represents the quickest convergence of all cases, reaching its optimum at epoch 12 with an MSE of approximately $5 * 10^{-4}$. The regression plot in Figure 11(c) indicates $R = 0.999$, which indicates a superior predictive agreement. Figure 11(d) shows that the training curve exhibits a gradual gradient reduction and a few data validation errors, which suggests that the curve represents stable learning without overfitting. In general, across all four cases, the Levenberg–Marquardt-trained neural network provides highly accurate predictions that are consistently reliable and exhibit good generalization capability, indicating its suitability as a surrogate model for complex nonlinear fluid, thermal, and concentration dynamics.



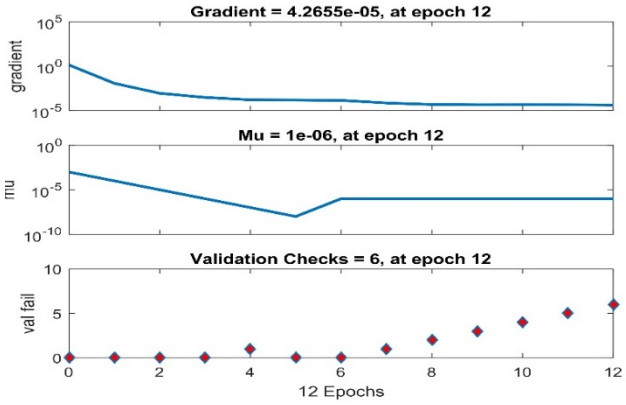
(a) Error bar plot for Cr.



(b) MSE plot for Cr.



(c) Regression plot for Cr.



(d) Training plot for Cr.

Figure 11. Artificial neural network performance evaluation for (Cr): (a) error histogram, (b) mean squared error (MSE), (c) regression analysis, and (d) training performance.

5. Conclusions

In the present work, the non-Newtonian Eyring–Powell fluid was investigated under the influence of a magnetic field, thermal radiation, and chemical reaction, and the numerical results demonstrated

physically consistent behavior across all boundary layers. The key findings are as follows:

i. Velocity increases as the stretching parameter, wedge angle, magnetic parameter, and Eyring–Powell parameter (K_1) increase. Also, velocity decreases as the parameter K_2 increases because of the increased effective viscosity and increased resistance to flow.

ii. Temperature increases with increasing radiation parameter, heat generation, thermophoresis parameter, and thermal Biot number, and decreases with increasing Prandtl number and wedge angle, which indicates more convective cooling.

iii. The Biot number and chemical reaction parameter increase the concentration, whereas the wedge angle decreases the concentration because mass convection becomes active.

iv. The magnetic parameter and wedge angle were identified by RSM and ANOVA as the most significant parameters influencing skin friction coefficient, while the residual analysis confirmed the statistical adequacy of the model.

v. The ANN trained using the Levenberg–Marquardt algorithm achieved very low minimum errors at approximately 10^{-9}. For the Eyring–Powell fluid parameters, the maximum errors were of the order 10^{-4}, while the thermal radiation and chemical reaction parameters exhibited maximum errors of the order 10^{-5}. The best validation performances were obtained at epochs 71, 126, 44, and 12.

vi. Regression values close to 1 indicate a strong agreement between the ANN predictions and the numerical values, demonstrating an excellent model fit. If the regression value is substantially lower than 1, the ANN architecture or training strategy may require further optimization.

vii. The sensitivity charts clearly illustrated the relative importance of each parameter and identified the dominant physical variables affecting skin friction coefficient, heat transfer, and mass transfer, thereby providing useful insights for engineering design and optimization.

5.1. Limitations of the study

The present study has several limitations related to both physical modeling and the adopted methodology. The effects of bioconvection and Fourier heat conduction are not considered. The present model also does not account for activation energy or dual-flow configurations. The sensitivity analysis is restricted to identifying the most influential parameters affecting skin friction coefficient. In addition, the ANN framework employs a conventional supervised machine-learning approach for flow prediction. Future studies may incorporate these physical effects and employ more advanced machine-learning techniques to further extend the present model.

5.2. Practical significance

The present findings are relevant to aerodynamic flow control and drag optimization over wedge-shaped surfaces. The key parameters influencing skin friction coefficient can be identified and utilized to regulate wall shear and improve aerodynamic performance. In particular, the magnetic parameter can be employed to control the flow velocity and boundary-layer behavior, while the rheological and wedge parameters provide additional means of regulating momentum transport. Furthermore, the ANN model enables rapid prediction of flow behavior without the need for repeated computationally expensive numerical simulations, thereby supporting efficient design, optimization, and engineering analysis.

Use of AI tools declaration

The authors declare they have not used Artificial Intelligence (AI) tools in the creation of this article.

Acknowledgments

The authors gratefully acknowledge the financial support from the National Natural Science Foundation of China (Grant No. 12502442). Further, the authors are grateful for the work of U. F.G. was partially supported by Government of the Basque Country: Elkartek KK-2024/00069, ELKARTEK25/28 and KK-2024/00117. Furthermore, the authors are grateful to King Saud University, Riyadh, Saudi Arabia, for funding the work through the Ongoing Research Funding program (ORF-2026-852).

Conflict of interest

Unai Fernandez-Gamiz is a guest editor for the special issue of the ERA and was not involved in the editorial review or the decision to publish this article. All authors declare that there are no competing interests.

References

1. I. E. Lagaris, A. Likas, D. I. Fotiadis, Artificial neural networks for solving ordinary and partial differential equations, *IEEE Trans. Neural Networks*, **9** (1998), 987–1000. https://doi.org/10.1109/72.712178
2. J. Ahmed, A. Shahzad, A. Begum, R. Ali, N. Siddiqui, Effects of inclined Lorentz forces on boundary layer flow of Sisko fluid over a radially stretching sheet with radiative heat transfer, *J. Braz. Soc. Mech. Sci. Eng.*, **39** (2017), 3039–3050. https://doi.org/10.1007/s40430-017-0759-z
3. T. Taha, Y. Fazeel, P. Kumam, T. Seangwattana, Intelligent modeling of nanoparticle transport in a permeable substrate with memory effects for cooling and heat exchange technologies, *Int. Commun. Heat Mass Transfer*, **178** (2026), 111628. https://doi.org/10.1016/j.icheatmasstransfer.2026.111628
4. N. Ijaz, A. Zeeshan, T. Taha, A. F. Hashem, Controlled AI for flow forecasting in Lorentz force dominance over power-index in streamline: Applications in catalytic cooling systems, *Int. Commun. Heat Mass Transfer*, **176** (2026), 111366. https://doi.org/10.1016/j.icheatmasstransfer.2026.111366
5. A. Zeeshan, M. I. Khan, R. Ellahi, Z. Asghar, Artificial neural network simulation and sensitivity analysis for optimal thermal transport of magnetic viscous fluid over shrinking wedge via RSM, *Int. J. Numer. Methods Heat Fluid Flow*, **33** (2023), 3492–3518. https://doi.org/10.1108/HFF-03-2023-0135
6. A. Zeeshan, N. Khalid, R. Ellahi, M. I. Khan, S. Z. Alamri, Analysis of nonlinear complex heat transfer MHD flow of Jeffrey nanofluid over an exponentially stretching sheet via three phase artificial intelligence and machine learning techniques, *Chaos, solitons Fractals*, **189** (2024), 115600. https://doi.org/10.1016/j.chaos.2024.115600

7. P. B. A. Reddy, R. Das, Estimation of MHD boundary layer slip flow over a permeable stretching cylinder in the presence of chemical reaction through numerical and artificial neural network modeling, *Eng. Sci. Technol. Int. J.*, **19** (2016), 1108–1116. https://doi.org/10.1016/j.jestch.2015.12.013
8. N. Islam, M. K. Abdalrahem, Z. Shah, B. S. Haji, A. A. Pasha, A. M. Minhas, et al., Intelligent mathematical modeling of non-Newtonian MHD nanofluid flow in Eyring–Powell systems for advanced thermal applications, *Chem. Eng. J. Adv.*, **27** (2026), 101376. https://doi.org/10.1016/j.ceja.2026.101376
9. S. S. Ali, R. Ellahi, A. Zeeshan, S. M. Sait, M. I. Khan, Computational investigation of MHD Eyring–Powell nanofluid boundary layer flow and heat transfer over a porous cylinder, *Int. J. Numer. Methods Heat Fluid Flow*, **2026** (2026. https://doi.org/10.1108/HFF-06-2026-0756
10. A. ur Rehman, Z. Asghar, A. Zeeshan, Optimal analysis of electro-osmotic peristaltic flow of Newtonian fluid through non-Darcy porous media via RSM and ANNs, *J. Porous Media*, **29** (2025). https://doi.org/10.1615/JPorMedia.2025056377
11. U. Naeem, M. Sohail, M. A. Sherani, F. Sultan, T. Taha, I. Mahariq, Cattaneo–Christov heat and mass fluxes impact on three-dimensional Williamson nanofluid flow over a stretching sheet utilizing artificial neural network analysis, *Multiscale Multidiscip. Model. Exp. Des.*, **8** (2025), 392. https://doi.org/10.1007/s41939-025-00980-3
12. R. Ali, N. Khalid, T. Taha, A. Mitalipova, A. Kurbanaliev, Polynomial degree impact on prediction accuracy in Casson-Williamson fluid with Cattaneo-Christov, *Results Eng.*, **26** (2025), 105068. https://doi.org/10.1016/j.rineng.2025.105068
13. N. Fatima, N. Ijaz, A. Zeeshan, T. Taha, N. Saleem, A. A. Hassaballa, Closed-loop AI control of nanoparticle transport under mixed convection: application to electromagnetic propulsion power generation, *Int. J. Mech. Mater. Des.*, **22** (2026), 132. https://doi.org/10.1007/s10999-026-09954-w
14. F. Wang, R. Parveen, S. Rehman, A. Farooq, H. Alhazmi, A. F. Aljohani, et al., Artificial neural computing and statistical analysis of heat and mass transport of nanofluid flow with melting heat and thermal stratification, *Case Stud. Therm. Eng.*, **60** (2024), 104563. https://doi.org/10.1016/j.csite.2024.104563
15. F. Wang, M. I. Asjad, M. Zahid, A. Iqbal, H. Ahmad, M. D. Alsulami, Unsteady thermal transport flow of Casson nanofluids with generalized Mittag–Leffler kernel of Prabhakar's type, *J. Mater. Res. Technol.*, 14 (2021), 1292–1300. https://doi.org/10.1016/j.jmrt.2021.07.029
16. F. Wang, S. Rehman, M. H. Shah, M. A. El Yamani, S. Farooq, A. Farooq, Numerical computation of cross nanofluid model using neural network and adaptive neuro-fuzzy inference system with statistical insights for enhanced flow optimization, *Expert Syst. Appl.*, **263** (2025), 125721. https://doi.org/10.1016/j.eswa.2024.125721
17. J. A. Jugnoo, A. ur Rehman, T. Taha, Non-Newtonian fluid flow with bioconvection: The role of Rayleigh number and buoyancy over a sheet, *J.Innovative Res. Math. Comput. Sci.*, **3** (2024), 91–107. https://doi.org/10.62270/jirmcs.v3i1.31
18. F. Sultan, M. Awais, M. Sohail, I. Mahariq, MHD and thermal effects on three-dimensional non-Newtonian Williamson fluid flow over a stretching sheet via numerical scheme, *ZAMM J. Appl. Math. Mech.*, **105** (2025), e70174. https://doi.org/10.1002/zamm.70174
19. M. Sohail, M. A. Sherani, K. Abodayeh, S. T. Abbas, Three-dimensional boundary layer dynamics of couple-stress non-Newtonian fluids: MHD effects and generalized flux analysis via OHAM, *ZAMM J. Appl. Math. Mech.*, **105** (2025), e70048. https://doi.org/10.1002/zamm.70048

20. A. S. Alqahtani, A. ur Rehman, Z. Asghar, A. Zeeshan, M. Y. Malik, Optimal analysis of MHD peristaltic flow of viscoplastic nanofluid with chemical reaction and electro-osmotic effect via artificial neural networks and response surface methodology, *Phys. Scr.*, **2024** (2024). https://doi.org/10.1088/1402-4896/ada18a
21. S. Ravikumar, B. Reddappa, O. D. Makinde, Understanding the chemical reaction, mixed convection, and thermo-diffusion features of non-Newtonian fluid (Prandtl fluid) driven by electroosmosis activity via wavy tapered microfluidic system, *Heat Transfer*, **54** (2025), 2305–2325. https://doi.org/10.1002/htj.23290
22. S. S. Zafar, U. Khan, F. Ali, S. M. Eldin, A. M. Saeed, A. Zaib, et al., Irreversibility analysis of radiative flow of Prandtl nanofluid over a stretched surface in Darcy-Forchheimer medium with activation energy and chemical reaction, *Heliyon*, **9** (2023), e14877. https://doi.org/10.1016/j.heliyon.2023.e14877
23. A. Zeeshan, Z. Asghar, A. U. Rehaman, AI based optimal analysis of electro-osmotic peristaltic motion of non-Newtonian fluid with chemical reaction using artificial neural networks and response surface methodology, *Int. J. Numer. Methods Heat Fluid Flow*, **34** (2024), 2345–2375. https://doi.org/10.1108/HFF-01-2024-0016
24. S. Samal, S. Ontela, S. Enamul, Optimization and sensitivity analysis in time-dependent magneto-hydrodynamic squeezing flow of radiative Eyring–Powell hybrid nanofluid with gyrotactic microorganisms: Entropy analysis, *ZAMM J. Appl. Math. Mech.*, **105** (2025), e70236. https://doi.org/10.1002/zamm.70236
25. M. M. Bhatti, A. Zeeshan, R. Ellahi, G. C. Shit, Mathematical modeling of heat and mass transfer effects on MHD peristaltic propulsion of two-phase flow through a Darcy-Brinkman-Forchheimer porous medium, *Adv. Powder Technol.*, **29** (2018), 1189–1197. https://doi.org/10.1016/j.apt.2018.02.010
26. A. ur Rehman, Z. Asghar, A. Zeeshan, Investigating the role of porous medium for frictional forces in peristaltic flow dynamics using ANN and RSM, *J. Porous Media*, **29** (2026), 1–24. https://doi.org/10.1615/JPorMedia.2025056377
27. S. Shafique, A. ur Rehman, A. Zeeshan, A. B. Mann, A. S. Alqahtani, M. Y. Malik, Empirical modeling and sensitivity analysis of thermal irreversibility and pressure rise in peristaltic flow using neural networks and response surface methodology, *Heat Transfer*, **55** (2026), 2600–2620. https://doi.org/10.1002/htj.70214
28. C. R. Mirza, Z. Shah, H. Iqbal, M. Jawaid, B. Dammak, Y. El Touati, et al., AI-RNN approach for radiative dissipative bioconvective flow of Eyring–Powell hybrid and ternary nanofluids, *Alex. Eng. J.*, **149** (2026), 113–128. https://doi.org/10.1016/j.aej.2026.06.022
29. S. S. Ali, R. Ellahi, A. Zeeshan, S. M. Sait, M. I. Khan, Computational investigation of MHD Eyring–Powell nanofluid boundary layer flow and heat transfer over a porous cylinder, *Int. J. Numer. Methods Heat Fluid Flow*, **2026** (2026), 1–28. https://doi.org/10.1108/HFF-06-2026-0756
30. C. N. Raju, C. S. Reddy, M. A. Alyami, S. M. Eldin, Adnan, K. K. Asogwa, et al., MHD Eyring–Powell nanofluid flow across a wedge with convective and thermal radiation, *Front. Energy Res.*, **10** (2022), 1021491. https://doi.org/10.3389/fenrg.2022.1021491
31. I. Ullah, S. Shafie, I. Khan, K. L. Hsiao, Brownian diffusion and thermophoresis mechanisms in Casson fluid over a moving wedge, *Results Phys.*, **9** (2018), 183–194. https://doi.org/10.1016/j.rinp.2018.02.021

32. C. S. K. Raju, M. M. Hoque, T. Sivasankar, Radiative flow of Casson fluid over a moving wedge filled with gyrotactic microorganisms, *Adv. Powder Technol.*, **28** (2017), 575–583. https://doi.org/10.1016/j.apt.2016.10.026



AIMS Press

©2026 the Author(s), licensee AIMS Press. This is an open access article distributed under the terms of the Creative Commons Attribution License (https://creativecommons.org/licenses/by/4.0)